



Non-linear response of glacier melting to Holocene warming in Svalbard recorded by sedimentary iron (oxyhydr)oxides

Kwangchul Jang^a, Germain Bayon^b, Christoph Vogt^c, Matthias Forwick^d, Youngkyu Ahn^a, Jung-Hyun Kim^a, Seung-Il Nam^{a,*}

^a Division of Glacial Environment Research, Korea Polar Research Institute, Incheon 21990, Republic of Korea

^b Univ Brest, CNRS, Ifremer, Geo-Ocean, F-29280 Plouzané, France

^c Crystallography & Geomaterials, FB05 Geosciences & MARUM, University of Bremen, 28359 Bremen, Germany

^d Department of Geosciences, UiT The Arctic University of Norway, NO-9037 Tromsø, Norway



ARTICLE INFO

Article history:

Received 23 August 2022

Received in revised form 9 February 2023

Accepted 12 February 2023

Available online xxxx

Editor: A. Jacobson

Keywords:

iron (oxyhydr)oxides

high Arctic environments

glacier retreat

tipping point

accelerated glacier melting

neodymium isotopes

ABSTRACT

The recent acceleration of ice-sheet loss with its direct impact on sea-level rise and coastal ecosystems is of major environmental and societal concern. However, the effect of atmospheric temperature increases on long-term glacier retreat remains poorly defined due to limited historical observations and uncertainties in numerical ice-sheet models, which challenges climate change adaptation planning. Here, we present a novel approach for investigating the time-transgressive response of Arctic glaciers since the last deglaciation, using glacially-derived Fe-(oxyhydr)oxide layers preserved in glacial marine sediments from a large fjord system in Svalbard. Glacial weathering releases large amounts of Fe, resulting in the deposition of Fe-(oxyhydr)oxide particulates in nearby marine sediments, which can serve as fossil indicators of past glacial melting events. Our results indicate that Svalbard glaciers retreated at a rate of 18 to 41 m/yr between 16.3 and 10.8 kyr BP, synchronously with the progressive rise in atmospheric and oceanic temperatures. From 10.8 kyr BP, glacier retreat markedly accelerated (up to ~116 m/yr) when regional atmospheric temperatures exceeded modern values. Coupled with field observations, this finding directly supports a non-linear response of glacial melting to summer air temperature increases. In addition to suggesting that ice-sheet loss and sea-level rise may further accelerate in the near future, this study paves the way for the use of sedimentary Fe-(oxyhydr)oxide layers in subarctic environments for reconstructing past glacial dynamics.

© 2023 The Author(s). Published by Elsevier B.V. This is an open access article under the CC BY license (<http://creativecommons.org/licenses/by/4.0/>).

1. Introduction

Global warming significantly impacts the cryosphere in modern Earth surface environments, resulting in the cumulative volume loss of ice sheets, glaciers, and sea ice (Howat and Eddy, 2011; Kochtitzky et al., 2022; Lindsay and Schweiger, 2015; Shepherd et al., 2018; Zemp et al., 2019). For instance, in Greenland, the average retreat rate of marine-terminating glaciers accelerated from 22 m/yr between 1985 and 2000 to 103 m/yr between 2000 and 2010 (Howat and Eddy, 2011). The mass loss of marine-terminating glaciers in the Northern Hemisphere further increased from 44.47 ± 6.23 Gt/yr between 2000 and 2010 to 51.98 ± 4.62 Gt/yr between 2010 and 2020 (Kochtitzky et al., 2022). This current global trend towards accelerating glacier mass loss leads to positive albedo feedback amplifying global warm-

ing (Flanner et al., 2011), as well as to massive freshwater runoff into the oceans, affecting sea-level rise (Rye et al., 2014), physical oceanography (Williams et al., 2016) and marine ecosystems (Fuentes et al., 2016).

Future climate projections based on general circulation models and various greenhouse gas emission scenarios (referred to as representative concentration pathways; RCPs) predict that ongoing ice melting will cause a global sea-level rise between 0.12–0.22 m (RCP2.6; i.e., a low emission pathway yielding a radiative forcing of 2.6 W/m² by 2100), and 0.15–0.26 m (RCP8.5; high emission pathway) by 2050, relative to the 1986–2005 period with a contribution by thermal expansion (Church et al., 2013; Oppenheimer et al., 2019). Such predictions on short timescales are associated with relatively small uncertainties, meaning that they can serve as an effective basis for establishing climate change adaptation strategies (Oppenheimer et al., 2019). However, over the long term, the projected sea-level rise varies substantially depending on RCPs, for instance, 0.30–0.65 m (RCP 2.6) and 0.63–1.32 m (RCP 8.5) by 2100

* Corresponding author.

E-mail address: sinam@kopri.re.kr (S.-I. Nam).

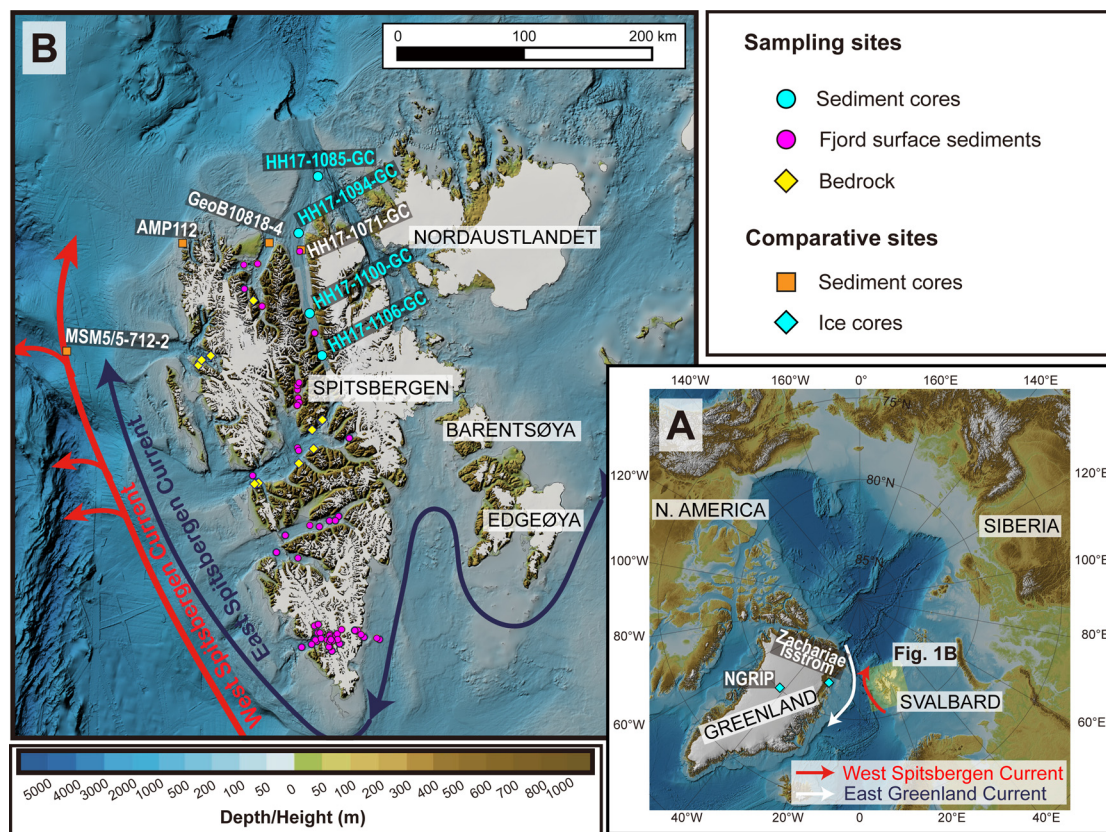


Fig. 1. Overview map of (A) the Arctic Ocean and (B) Svalbard archipelago. Sampling locations for sediment and bedrock samples analysed in this study are marked with sky blue circles and yellow diamonds, respectively, in (B). The comparative sites and oceanic currents mentioned in the text are shown. Seafloor morphology was constructed based on the IBCAO 4.0 bathymetric grid (Jakobsson et al., 2020), with additional bathymetric information in Wijdefjorden (Allaart et al., 2020).

and 0.54–2.15 m and 1.67–5.61 m by 2300 (Horton et al., 2020). Such large uncertainties mostly reflect our limited understanding of the dynamics of polar glaciers and ice sheets, requiring quantitative constraints on the future evolution of the cryosphere and associated sea-level rise based on palaeo-analogues.

In this study, we present a novel approach for quantifying the rate of glacier mass loss in response to past global warming based on the identification of iron (Fe) (oxyhydr)oxide (defined as the sum of Fe-oxide and Fe-oxyhydroxide; hereafter FeOx) layers in glacial marine sediment records. Bedrock geology and/or hydrological conditions below glaciers are known to influence the distribution of FeOx in high-latitude fjord sediments (Wehrmann et al., 2014). However, glacial meltwaters deliver massive amounts of iron released from erosional and biogeochemical weathering processes at the base of ice sheets and other glacial masses (Hawkings et al., 2020, 2014), which settles mostly down in ice-proximal environments through the estuarine process (Boyle et al., 1977; Raiswell et al., 2018; Schroth et al., 2014; Zhang et al., 2015). Therefore, distinctive enrichments of FeOx in well-dated sediment records surrounding glaciated catchments potentially serve as novel diagnostic features for past glacial melting events from adjacent glaciers, hence providing insights into the dynamics of glacier retreat in response to climate change. Here, we apply this concept to glacial marine sediment records collected along a latitudinal N–S transect in northern Svalbard, a glaciated archipelago in the Arctic Ocean (Fig. 1). Our main objective is to characterize the spatial and temporal evolution of Svalbard ice masses during and after the last deglaciation. We will provide evidence below that glacier melting during the early Holocene responded non-linearly to climate warming.

2. Study area

The Svalbard archipelago is composed of multiple fjord systems formed as a result of repeated glacier activity in the past (Fig. 1). Because of the northward intrusion of warm Atlantic Water (AW) carried by the West Spitsbergen Current, Svalbard is relatively warmer than other high-latitude regions and is thus more directly impacted by the current global warming (Isaksen et al., 2007 and references therein). Three main water masses dominate the hydrographic setting in Svalbard fjords, which include AW, cold Arctic water and terrestrial meltwater flow (Cottier et al., 2010).

The bedrock geology of Svalbard is very diverse, displaying markedly differing lithological compositions from one fjord to another (Dallmann and Elvevold, 2015). Hornsund bedrock ranges from west to east from Proterozoic metamorphic rocks to Palaeogene sedimentary rocks, while Dicksonfjorden and Woodfjorden are both dominated by the Devonian Old Red Sandstone. Wijdefjorden displays contrasted bedrock geology in western and eastern catchment areas, which are dominated by the Devonian Old Red Sandstone and Proterozoic to lower Silurian metamorphic rocks, respectively.

Svalbard has undergone repeated phases of glacier advances and retreats during and after the last glacial period (Hughes et al., 2016). During the last glacial maximum, the archipelago was almost entirely covered by the Svalbard-Barents Sea Ice Sheet (SBIS), which began to retreat from the continental shelf edges in northern and western Svalbard ca. 19 kyr BP (Hughes et al., 2016 and references therein). In northern Svalbard, the continental shelf off Wijdefjorden and the fjord mouth of Wijdefjorden were deglaciated prior to ca. 16.3 kyr BP (Jang et al., 2021) and 14.5 kyr BP (Allaart et al., 2020), respectively. The deglaciation on the outer part of Wijdefjorden occurred after ca. 12 kyr BP (Hughes et

al., 2016), and most land-based glaciers had vanished by 7.6 kyr BP (Allaart et al., 2020). The glacial coverage reached its minimum extent during the Holocene Thermal Optimum (ca. 11.2–5.2 kyr BP) (Farnsworth et al., 2020). Svalbard glaciers readvanced throughout the Late Holocene in response to regional cooling, many of them reaching their maximum post-glacial extents during the Little Ice Age (Svendsen and Mangerud, 1997; Werner, 1993).

3. Materials and methods

3.1. Sample collection

In this study, we used various bedrock ($n = 18$), fjord surface sediment ($n = 62$) and core sediment (four cores; $n = 334$) samples from Svalbard. Bedrock samples include two metamorphic rocks and sixteen sedimentary rocks collected from representative bedrock units of Svalbard (for details, see Jang et al., 2020). A series of fjord surface sediments were collected from various Svalbard fjord systems during RV *Helmer Hanssen* expeditions (UiT The Arctic University of Norway) between 2012 and 2019 (Fig. 1). Four gravity cores were retrieved along a 150 km long N–S transect from the continental shelf off northern Svalbard to the innermost Wijdefjorden: core HH17-1085-GC (hereafter 1085; 80.27°N, 16.21°E, 322 m water depth; continental shelf), HH17-1094-GC (hereafter 1094; 79.74°N, 15.42°E, 148 m water depth; fjord mouth), HH17-1100-GC (hereafter 1100; 79.30°N, 15.78°E, 112 m water depth; central fjord), and HH17-1106-GC (hereafter 1106; 79.00°N, 16.21°E, 160 m water depth; inner fjord) (for locations, see Fig. 1 & Supplementary Table S1).

3.2. AMS ^{14}C age dating

The age model for core 1085 was previously constructed using various AMS radiocarbon data ($n = 12$; Jang et al., 2021). In this study, new AMS ^{14}C data were obtained for marine mollusc shells from cores 1094 ($n = 8$), 1100 ($n = 1$), and 1106 ($n = 4$), analysed at the BETA Analytic Laboratory (Miami, USA) and the Alfred Wegener Institute, Helmholtz Centre for Polar and Marine Research (Bremerhaven, Germany) (Supplementary Table S2). In addition to previous radiocarbon data ($n = 4$) for core 1100 (Braun, 2019), all measured ^{14}C ages were converted to calendar ages based on the Marine13 dataset of the Calib Rev 7.0.4 program (Stuiver and Reimer, 1993) with a marine reservoir offset $\Delta R = 105 \pm 24$ yr (Mangerud et al., 2006). For consistency with the previously published age model for core 1085 (Jang et al., 2021), a Bayesian age-depth model (BACON, v.2.2) (Blaauw and Christen, 2011) was used to determine the age-depth relationship in cores 1094, 1100 and 1106 with the default setting, except for the Student's t -distribution parameters t_a and t_b , which were switched from 3 and 4 to 33 and 34, respectively, in order to include all measured radiocarbon ages (Jang et al., 2021).

3.3. Mineralogical analyses

X-ray diffractograms were measured on all powdered bedrock ($n = 18$), fjord surface sediment ($n = 62$) and core sediment ($n = 334$) samples ($<20 \mu\text{m}$ particle size) using a Philips X'Pert Pro multipurpose diffractometer equipped with a Cu-tube ($k\alpha$ 1.541, 45 kV, 40 mA), a fixed divergence slit of $1/4^\circ$, a 16 samples changer, a secondary Ni filter and the X'Celerator detector system at the University of Bremen, Germany. A continuous scan was conducted from $3\text{--}85^\circ 2\theta$ with a calculated step size of $0.016^\circ 2\theta$ (calculated time per step was 50 seconds). The main mineral assemblages were generally identified with the Philips software X'Pert HighScore™, but for sheet silicates with the freely available Apple Macintosh X-ray diffraction interpretation software MacDiff

4.25 (Petschick et al., 1996). The quantification of mineral phases was achieved through the QUAX full-pattern method using a reference material database (Vogt et al., 2002). The mineralogical composition of studied samples is dominated by carbonate, quartz, feldspar, clay minerals and various accessory minerals. Crystalline FeOx including haematite, goethite, lepidocrocite and magnetite were identified and quantified based on an extensive pure mineral database. Note that FeOx (mostly Fe-oxyhydroxide) also occurs as amorphous phases in Svalbard sediment cores that cannot be recognized with X-ray diffractograms. In most samples, a single crystalline FeOx mineral phase is dominant with the other near the determination limits. As a consequence, FeOx abundances in this study are reported as the sum of recognized FeOx except for magnetite. According to the internal analytical quality test using the prepared mixtures including the Reynolds Cup samples at the XRD laboratory (e.g., Raven and Self, 2017), the relative error (1 SD) on measured FeOx contents was better than 10% (for example, 10 ± 1 wt%). Well-crystallized minerals such as quartz, calcite, aragonite, pyrite and some FeOx including haematite and magnetite were determined with uncertainties less than 1–3% when testing on simple artificial mixtures (Vogt et al., 2002). Values for FeOx are reported in Supplementary Tables S3–S8, and full report of the mineralogical abundances can be accessed from the PANGAEA databank (<http://www.pangaea.de>).

3.4. Geochemical analyses

Total organic carbon (TOC) contents and $\delta^{13}\text{C}_{\text{org}}$ compositions were determined in bulk sediments at cores 1094, 1100 and 1106 using an isotope ratio mass spectrometer (Delta V, Thermo Scientific) connected to an elemental analyser (Flash 2000, Thermo Scientific) at the Korea Polar Research Institute. Prior to analyses, bulk sediments were powdered to $<20 \mu\text{m}$ and then acidified with 2 M HCl on a funnel shaker for ~ 24 hours to remove inorganic carbon. The $\delta^{13}\text{C}_{\text{org}}$ values are expressed relative to the Vienna Pee Dee Belemnite (VPDB) reference value. Duplicate analyses of $\delta^{13}\text{C}_{\text{org}}$ on the randomly selected samples represent an average standard deviation of less than 0.2‰.

4. Results

4.1. Age models

The AMS ^{14}C ages and converted calendar ages in cores 1094, 1100 and 1106 are reported in Supplementary Table S2. Note that the AMS dates for core 1094 record two minor (< 1 kyr) age inversions at 24.5–30 cm and 55–65 cm sediment depths (Fig. 2). Nevertheless, all AMS dates were used for the determination of the age-depth relationship by Bayesian analysis (Blaauw and Christen, 2011), consistent with the previous age model determined for core 1085 (Jang et al., 2021). The consequent weighted mean values were used to determine the age-depth relationship (Fig. 2). Sedimentation at cores 1094, 1100, and 1106 covers the last 15.0, 14.1, and 4.5 kyr BP, corresponding to average sediment accumulation rates of 28.0, 26.7 and 89.5 cm/kyr, respectively. The basal ages of all cores are extrapolated. It should be noted that the basal ages of cores 1094 and 1100 should be treated with caution due to the absence of dating material in the lowermost parts of both cores (Fig. 2). However, this uncertainty does not affect the glacier retreat rates discussed below because they fall within the depths where dating material was available.

4.2. FeOx contents

Most Svalbard bedrock samples analysed in this study contain negligible amounts of FeOx minerals (Supplementary Table

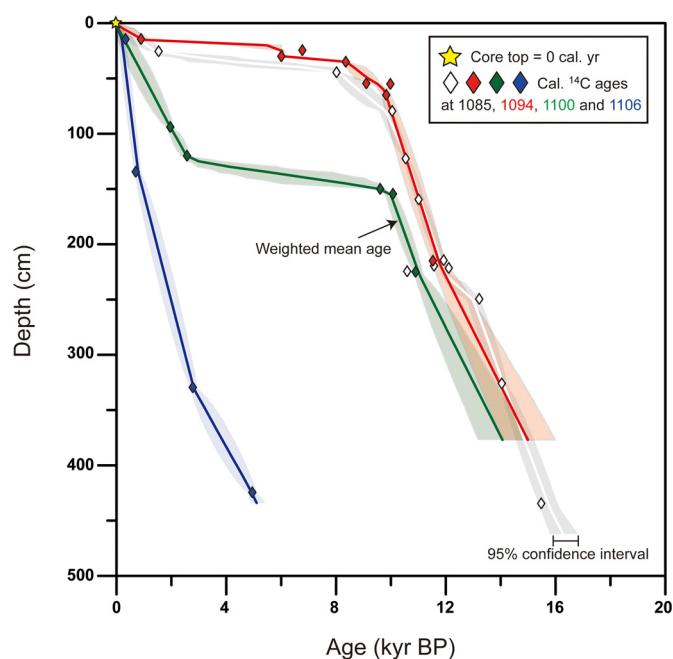


Fig. 2. Age models for cores HH17-1094-GC, HH17-1100-GC and HH17-1106-GC compared with that for HH17-1085-GC. Calibrated ^{14}C ages were used to determine the age-depth relationship based on Bayesian statistics in BACON (v. 2.2) (Blaauw and Christen, 2011).

S3). Exceptions are a Triassic black mudstone (0.4 wt%; sample ID 080111), the Devonian Old Red Sandstone (0.5 wt%; sample ID 080302), a Carboniferous sandstone (1.0 wt%; sample ID 13071005), and an Upper Proterozoic phyllite (1.3 wt%; sample ID 13071105). In most cases, haematite is the predominant FeOx species and the other FeOx minerals are rarely present as below the determination limits.

The FeOx contents of surface sediments in Svalbard fjords exhibit large spatial variability, ranging from 0 to 17.3 wt% (Fig. 3A). In Hornsund, where bedrock geology is highly diverse, the distribution of FeOx contents in surface sediments is most variable (Fig. 3B & Supplementary Fig. S1), and haematite and/or goethite represent the dominant FeOx phases (Supplementary Table S4). The maximum FeOx content (~ 17.3 wt%) is observed in the inner part of Wijdefjorden (Fig. 3C). Comparable FeOx values are also encountered in Dicksonfjorden and the inner part of Woodfjorden. The FeOx contents in these three different fjords exceed those of associated source rocks (Jang et al., 2020, 2021), such as the Devonian Old Red Sandstone (0.5 wt%). In these fjords, haematite represents the dominant FeOx species in surficial sediments (Supplementary Table S4). In general, FeOx contents in surface sediments tend to decrease away from sediment sources near glacier fronts. This trend can be observed in Wijdefjorden, where a pronounced seaward decrease in FeOx contents, from 17.3 to 0 wt%, occurred from the inner to the outer part of the fjord (Fig. 3C).

Core sediments in Wijdefjorden display significant downcore FeOx variability (Figs. 4 and 5). At site 1085, FeOx concentrations remained high (maximum 12.4 wt%) between 16.3 and 12.3 kyr BP and then dropped significantly and remained below 1.4 wt% since then (Fig. 4). Likewise, the FeOx contents at the other studied sites generally showed higher values before the Holocene but became nearly absent after 10.8 (site 1094) and 10.4 kyr BP (site 1100) (Fig. 5). The FeOx reappeared at the southernmost sites 1100 and 1106, approximately 4000 years ago. Haematite is generally the dominant FeOx species in all sediment cores, but goethite together with haematite are also predominant in the upper part of cores 1085 and 1094 where FeOx contents are relatively small (Supplementary Tables S5–S8).

4.3. TOC contents and $\delta^{13}\text{C}_{\text{org}}$ values

The TOC contents and $\delta^{13}\text{C}_{\text{org}}$ values of bulk sediments in cores 1094, 1100 and 1106 are reported in Supplementary Table S9. Compared to the average TOC content in core 1085 (0.5 ± 0.2 wt%, 1 SD, $n = 99$; Jang et al., 2021), cores 1094 and 1106 show slightly lower values of 0.4 ± 0.2 wt% (1 SD, $n = 77$) and 0.3 ± 0.1 wt% (1 SD, $n = 80$), respectively, while core 1100 represents a comparatively higher TOC average of 1.0 ± 0.4 wt% (1 SD, $n = 75$). Similar to core 1085, there is an overall upward increasing trend in core 1094 (Supplementary Fig. S2). On the other hand, core 1100 shows an upward decrease in TOC contents, while TOC values remain largely constant in core 1106 (Fig. 6). The average $\delta^{13}\text{C}_{\text{org}}$ values for cores 1094, 1100 and 1106 are $-24.2 \pm 1.0\text{‰}$ (1 SD, $n = 77$), $-22.9 \pm 0.3\text{‰}$ (1 SD, $n = 75$) and $-22.0 \pm 0.4\text{‰}$ (1 SD, $n = 80$), respectively, which are relatively higher than those for core 1085 ($-24.2 \pm 1.0\text{‰}$, 1 SD, $n = 99$; Jang et al., 2021) (Fig. 6). In general, sediments deposited during the Holocene tend to have relatively higher $\delta^{13}\text{C}_{\text{org}}$ signatures compared to other late Pleistocene sediments (Fig. 6).

5. Discussion

5.1. Factors controlling the distribution of FeOx contents

As mentioned earlier, hydrological conditions and/or bedrock geology are generally considered the two main factors controlling the distribution of FeOx in high-latitude fjord sediments (Wehrmann et al., 2014). In this study, the most pronounced FeOx enrichments in surface sediments are observed in Dicksonfjorden and the inner parts of Woodfjorden and Wijdefjorden (Fig. 3A). At present, glacio-fluvial rivers are dominant in Dicksonfjorden, while tidewater glaciers also exert a strong influence on Woodfjorden and Wijdefjorden. These highly contrasted hydrological settings suggest that the FeOx enrichments do not appear to be controlled by local hydrological or hydrodynamic conditions (e.g., land vs. marine-terminating glacier systems).

In these three fjord systems, bedrock geology is dominated by the Devonian Old Red Sandstone (Dallmann and Elvevold, 2015) (Fig. 3A). Evidence for the presence of reddish sediments and haematite-dominated FeOx in these fjords also points towards the Devonian Old Red Sandstone as a dominant sediment source. This assumption is further supported by the fact that detrital surface sediments in Dicksonfjorden, Woodfjorden and Wijdefjorden all display similar Nd isotopic compositions (hereafter detrital ε_{Nd}), i.e., hence indicating similar provenance (Jang et al., 2020). Likewise, the larger FeOx variability observed in Hornsund surface sediments reflects the more diverse bedrock geology in this latter fjord (Fig. 3B).

All the above consideration suggests that FeOx distribution in Svalbard surface sediments is mostly governed by corresponding source rocks (Wehrmann et al., 2014). However, the degree of FeOx enrichment in surface fjord sediments far exceeds that of surrounding source rocks in the catchment areas (i.e., ~ 0.5 wt% for the Devonian Old Red Sandstone). Given that we only used a single bedrock sample to represent the bedrock geology near Dicksonfjorden, Woodfjorden and Wijdefjorden, the potential input from FeOx-enriched deposits cannot be excluded.

The proximity to glacier fronts most likely represents an additional important factor that governs sedimentary FeOx contents (Fig. 6). This is illustrated in Hornsund, where the proportion of sedimentary FeOx generally decreases with increasing distance from glacier termini (Fig. 3B & Supplementary Fig. S1). The same observation can be made in Wijdefjorden, where sedimentary FeOx contents progressively decrease from the inner to the central part

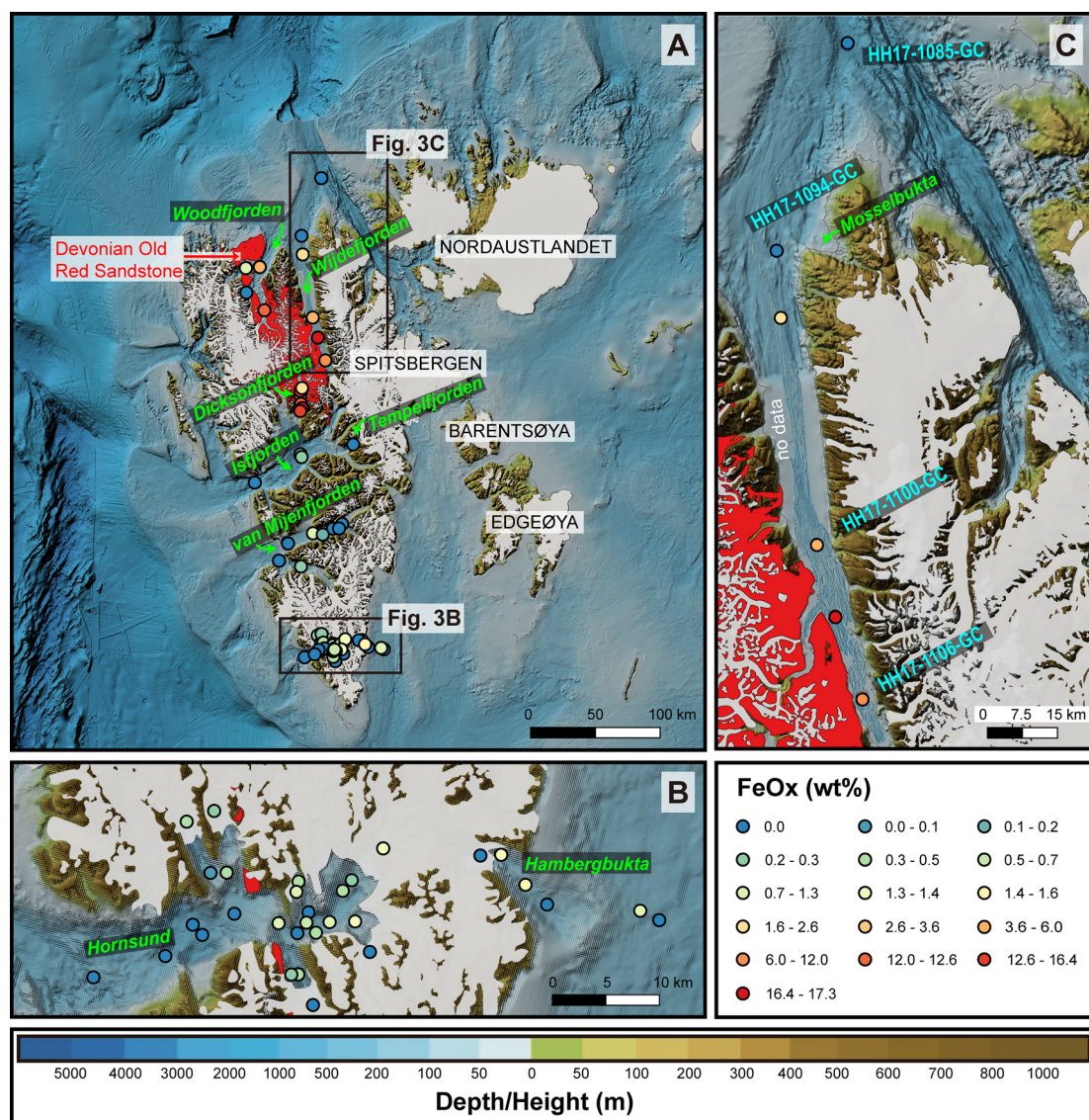


Fig. 3. Spatial distribution of Fe-(oxyhydr)oxide minerals (FeOx; weight percentage) in (A) Svalbard, (B) Hornsund and (C) Wijdefjorden. The FeOx contents are shown by coloured circles. The coverage area of the Devonian Old Red Sandstone in Svalbard (red) is shown for comparison (Dallmann and Elvevold, 2015).

of the fjord (Fig. 3C), without any concomitant change in sediment provenance, as inferred from similar detrital ε_{Nd} (Jang et al., 2020). These observations are consistent with the evidence that glacial meltwaters deliver substantial amounts of iron to proximal marine environments in Svalbard and other polar regions (Hawkins et al., 2020, 2014; Kanna et al., 2020). The glacially-derived iron contained in meltwater plumes is mostly removed in the low-salinity region through particle settling (Schroth et al., 2014) as well as colloidal flocculation and FeOx precipitation (Boyle et al., 1977; Kanna et al., 2020; Meslard et al., 2018; Zhang et al., 2015). In Svalbard, this process likely leads to the accumulation of FeOx layers in fjord sediments.

5.2. Sedimentary FeOx as archives of past meltwater discharges

The potential of sedimentary FeOx to reconstruct past ice sheet/glacier retreat can be tested on core 1085 from the continental shelf off northern Svalbard (for location, see Fig. 1). This core provides a continuous record of the palaeoenvironmental conditions offshore northern Svalbard over the past ~ 16.3 kyrs (Jang et al., 2021), including the occurrence of proximal glacial marine sediments deposited during the retreat of the Svalbard-Barents Ice

Sheet (SBIS) that entirely covered Svalbard during the last glacial maximum (Hughes et al., 2016). At site 1085, FeOx concentrations were generally higher, reaching a maximum of 12.4 wt% between 16.3 and 12.3 kyr BP, but underwent a significant decline to nearly undetectable levels since then. (Fig. 4). The observed FeOx decrease after 12.3 kyr BP coincides with the disappearance of sedimentary lamination (Fig. 4), i.e., a characteristic diagnostic feature of glacial marine sedimentation induced by suspension settling from meltwater plumes emanating from glacier fronts (Ó Cofaigh and Dowdeswell, 2001). Taken together, the combined evidence for a decrease in FeOx contents and the disappearance of laminae in core 1085 after 12.3 kyr BP indicates a change from ice-proximal to ice-distal depositional environments at that time (Jang et al., 2021). This interpretation is consistent with the lack of evidence for glacier readvance on northern Svalbard during the Younger Dryas (Allaert et al., 2020; Bartels et al., 2017; Jang et al., 2020). Importantly, the observed change in FeOx contents is unlikely to be explained by a switch in sediment provenance after 12.3 kyr BP because corresponding detrital ε_{Nd} values indicate no major compositional changes at this site throughout this transitional period (Fig. 4).

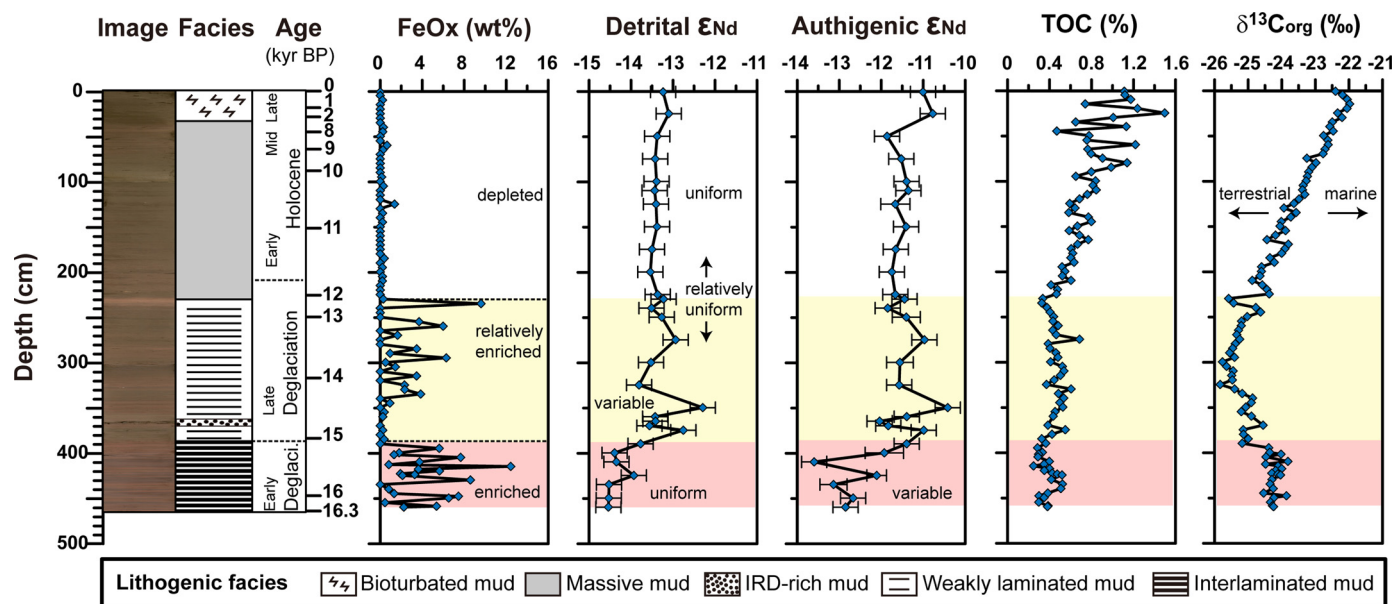


Fig. 4. Temporal variation in the contents of Fe-(oxyhydr)oxides (FeOx) in core HH17-1085-GC on the continental shelf off northern Svalbard. The data are compared with lithological facies, detrital and authigenic neodymium isotopes, and contents and isotopic compositions of total organic carbon (TOC) (Jang et al., 2021). The enrichments in FeOx occur in interlaminated (reddish area) and weakly laminated (yellowish area) muds, while the depletions occur in massive and bioturbated muds.

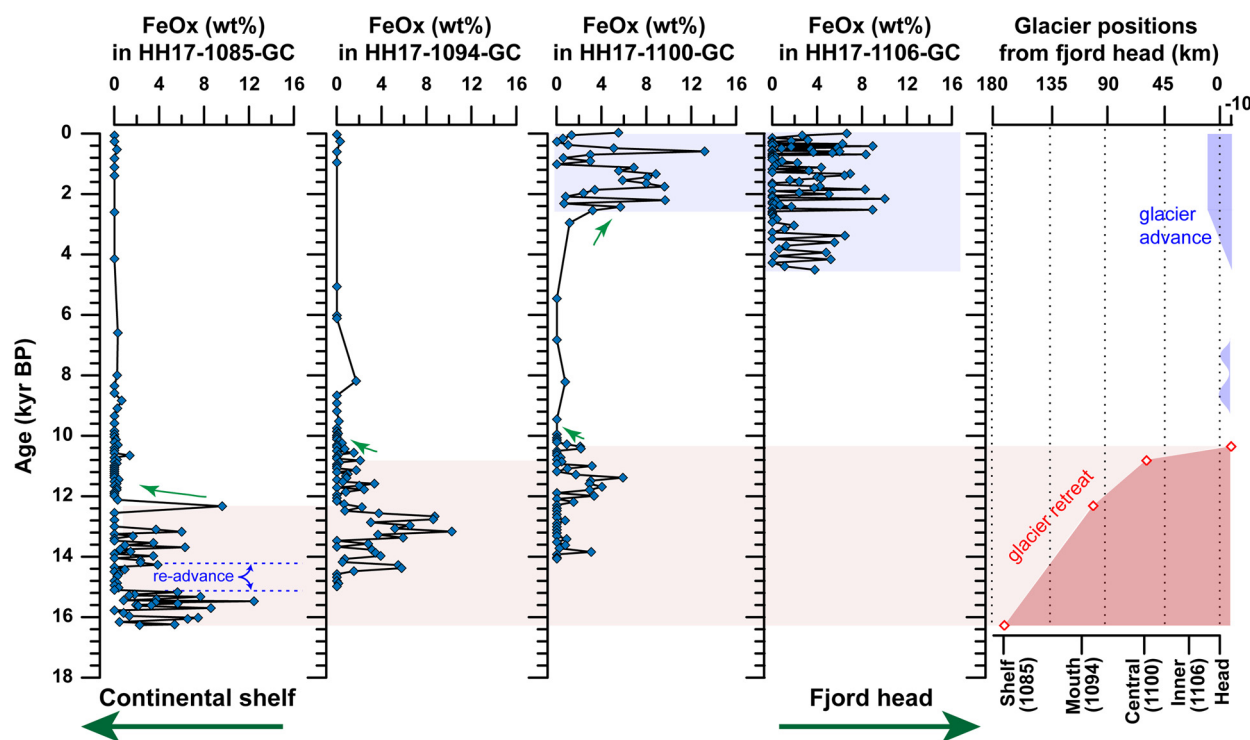


Fig. 5. Glacier positions reconstructed by temporal and spatial variability of FeOx in core sediments collected along a latitudinal transect on northern Svalbard. The transition from abundant to near-absent FeOx deposition in each core indicates a significant drop in glacially-derived iron related to the retreat of glacier fronts. The dotted horizontal blue lines in the left panel indicate the periods when glacier re-advance occurred (Jang et al., 2021). Note that glacier positions during the postglacial period are subject to some uncertainty that relates to the effective distance for iron delivery and deposition in fjord sediments (see text for details).

Therefore, we interpret the pronounced FeOx decrease after 12.3 kyr BP to reflect the major retreat of the nearby glacier front (compare with Allaart et al., 2020), resulting in significantly reduced deposition of glacially-derived Fe-bearing particulates onto the continental shelf offshore northern Svalbard (Fig. 6). Following glacier retreat, it is likely that the deposition of glacially-derived sedimentary FeOx migrated to more proximal inner fjord areas, thereby explaining their absence on the distant outer shelf. This interpretation is fully consistent with other lithological and geo-

chemical evidence from sediment records in northern Svalbard (Allaart et al., 2020; Jang et al., 2021), which also suggests an overall retreat of the SBIS from the continental shelf into the inner fjords during the last deglaciation.

It is worth noting that FeOx displays up and down variability at site 1085 during the early stage of deglaciation, despite again exhibiting relatively unchanged detrital ϵ_{Nd} compositions (Fig. 4). While this observation could be possibly interpreted as reflecting the alternation of short-lived events of glacier advances and re-

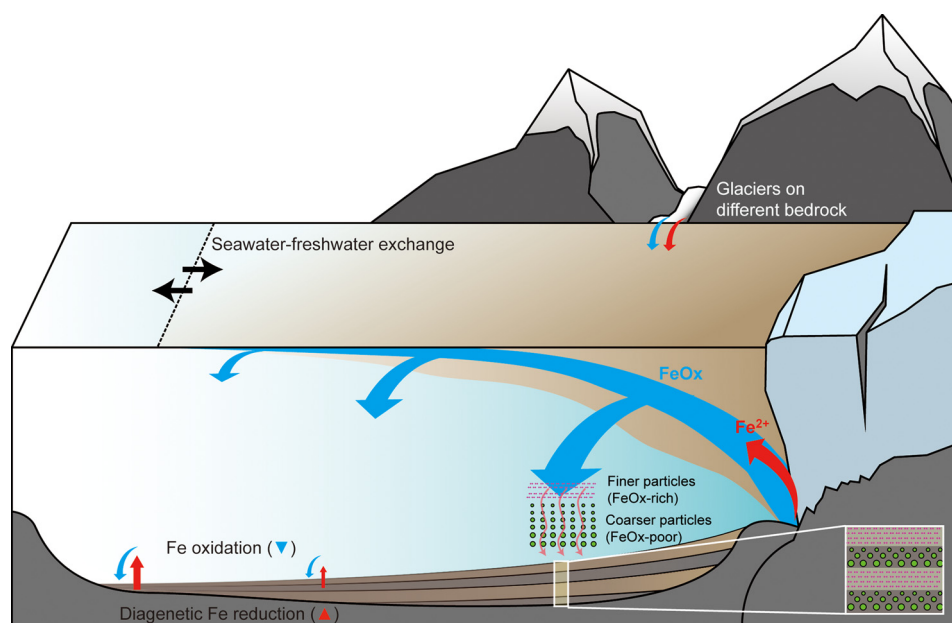


Fig. 6. Conceptual model for the fate of glacially-derived particulate (FeOx; blue) and dissolved (Fe^{2+} ; red) iron upon mixing with seawater. The deposition of glacially-derived iron is primarily governed by the position of the glacier margin, resulting in FeOx-enriched sediments in ice-proximal environments. The initial iron flux from glaciers depends on the underlying bedrock geology, and the diagenetic iron flux depends on the amount of labile marine organic matter. The sediment structure changes from laminated to massive with increasing distance from the glacier front.

treats, an alternative explanation would be that it relates to the cyclic formation of a couplet composed of a coarse-grained layer (i.e., Fe-poor) overlain by a finer-grained layer (i.e., Fe-rich) (Fig. 6), reflecting size-dependent settling of suspended particulates during each major meltwater discharge, i.e., a characteristic diagnostic feature of laminated glacial marine sedimentation (Cowan and Powell, 1990; Jang et al., 2021; Ó Cofaigh and Dowdeswell, 2001) (Fig. 4). Additionally, complex interactions between meltwater vs. seawater masses and their mixing could also possibly account for such FeOx variability in fjord deglacial sediments (for details, see section 5.3). On the other hand, the absence of any significant FeOx deposition during the ~ 15.0 – 14.3 kyr BP time interval could reflect a change in sediment source areas from the Fe-rich northwestern Svalbard to the Fe-poor northeastern Svalbard, as inferred from a prominent rise in detrital ε_{Nd} signatures (Jang et al., 2021) (Fig. 4).

5.3. Evaluating additional hydrological and diagenetic controls on FeOx distribution

Glaciers and ice sheets supply abundant material via surface runoff, resulting in the export of sediment-laden subglacial water plumes acting as a primary Fe source to the nearby marine environment (Hawkings et al., 2014, 2020; Wadham et al., 2019) (Fig. 6). Glacially-derived iron is mainly present as particulate FeOx (Schroth et al., 2014), together with a minor component of ‘dissolved’ iron (mostly in colloidal and nanoparticulate forms; Raiswell et al., 2018). The vast majority of glacially-derived iron is deposited under ice-proximal environments, following removal in the low-salinity region through estuarine flocculation, i.e., at the interface between seawater and freshwater (Boyle et al., 1977; Raiswell et al., 2018; Schroth et al., 2014; Zhang et al., 2015). Particulate FeOx can be further transported along with meltwater plumes, but also mostly settles in brackish environments (Schroth et al., 2014). The physical mixing between seawater and glacial meltwater typically results in complex hydrodynamics in fjords, which can strongly influence the location of particulate FeOx deposition in the marine environment (Raiswell et al., 2018) (Fig. 6). For instance, such complex hydrodynamics in Svalbard fjords could possibly account for the relatively large Nd isotope variability in

the leached hydrogenous FeOx fractions (hereafter authigenic ε_{Nd}) at Site 1085 before ca. 14 kyr BP, i.e., a tracer of water mass mixing (Jang et al., 2021) (Fig. 4). Considering that terrestrial meltwater and ambient seawater at the continental shelf off northern Svalbard display distinctive Nd isotope compositions (Jang et al., 2021), the observed authigenic ε_{Nd} variability during that time interval could reflect short-term variations in the mixing between those water sources, thereby possibly explaining the observed FeOx evolution downcore. Nevertheless, the fact that authigenic ε_{Nd} signatures remain nearly constant after 14 kyr BP (Jang et al., 2021) (Fig. 4), hence being completely decoupled from the evolution of FeOx contents, suggests that local hydrodynamic changes are unlikely to have driven the downcore evolution of sedimentary FeOx contents at Site 1085 on the continental shelf off Wijdefjorden.

FeOx enrichment along the core could also reflect the influence of diagenetic Fe reduction (Fig. 6), which occurs in suboxic marine sediments, resulting in substantial benthic fluxes of Fe to overlying water masses (Laufer-Meiser et al., 2021; Tessin et al., 2020; Wehrmann et al., 2014). In marine sediments, the upward-migrating flux of diagenetic Fe is oxidized at the suboxic-oxic boundary near the seawater-sediment interface, leading to the precipitation of authigenic FeOx minerals (Laufer-Meiser et al., 2021; Wehrmann et al., 2014) (Fig. 6). Such process could possibly explain the observed FeOx enrichment at site 1085. However, at site 1085, the general upward increase in both TOC contents and $^{13}\text{C}_{\text{org}}$ values points towards the enhanced contribution of fresh marine organic matter (e.g., Jang et al., 2021; Knies and Martinez, 2009) (Fig. 4), indicating that diagenetic Fe cycle may have progressively intensified through time at this particular site (Laufer-Meiser et al., 2021; Wehrmann et al., 2014). This is in marked contrast with the observation that FeOx contents at site 1085 are much smaller in the upper, organic-rich, sediment layers (Fig. 4), hence suggesting minor diagenetic controls on sedimentary FeOx downcore. Note also that the abundance of sedimentary FeOx and TOC contents does not display any particular relationship in all studied cores ($0.00 < r^2 < 0.18$) (Supplementary Fig. S2), providing further evidence for the minor diagenetic control on the downcore variability of FeOx in this study.

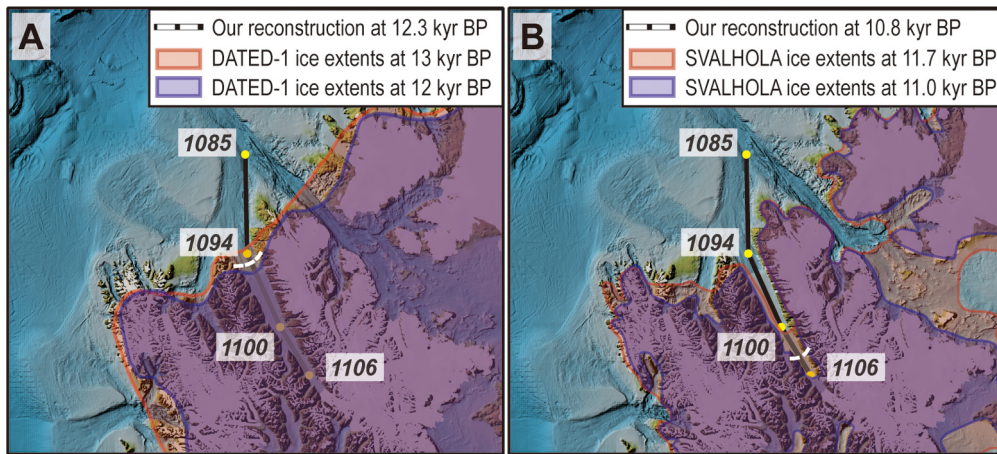


Fig. 7. Tentative ice extents at 12.3 and 10.8 kyr BP recorded by the spatio-temporal variability of FeOx in cores HH17-1085-GC, HH17-1094-GC, HH17-1100-GC and HH17-1106-GC. (A) The estimated ice extent at 12.3 kyr BP is well-matched with the previous reconstruction of the most-incredible DATED-1 timeslices at ~13 and 12 kyr BP (Hughes et al., 2016). (B) The ice reconstruction at 10.8 kyr BP shows slightly more expanded coverage than the recent reconstructions at 11.0 kyr BP based on the SVALHOLA database (Farnsworth et al., 2020) but much larger extent than the most-incredible DATED-1 timeslices at 11 kyr BP, which showed complete deglaciation in inner Wijdefjorden (Hughes et al., 2016). Note that the ice at 10.4 kyr BP is suggested to have retreated landward, which is consistent with the previous reconstructions.

To summarize, despite the potential influences of both early diagenetic processes and hydrodynamic changes on the cycling of particulate FeOx in Svalbard fjords, that these processes probably played a minor role in controlling the observed distribution of FeOx layers along the studied cores. This provides reassuring evidence that FeOx can serve as a useful proxy for tracking meltwater discharges and the proximity of past glacier fronts to Svalbard fjords.

5.4. Reconstruction of the glacier retreat pattern during the last deglaciation

The novel FeOx proxy was applied to four well-dated sediment records along an ~150 km long N–S transect in Wijdefjorden, the longest fjord system in northern Svalbard: cores 1085, 1094, 1100, and 1106 (for location, see Fig. 1). This novel spatio-temporal approach allows a detailed reconstruction of the dynamics of the SBIS during the last deglaciation, as well as the evolution of local glaciers during post-glacial times. All studied sediment records display significant down-core FeOx variability (Fig. 5), including the timing of the FeOx maximum at each study site, which we interpret here as marking the time-transgressive termination of local peak meltwater discharges during the last deglaciation. The respective maxima occurred at 15.5 (site 1085), 13.2 (site 1094), and 11.7 kyr BP (site 1100), reflecting the progressive landward retreat of the SBIS during deglaciation (Farnsworth et al., 2020; Hughes et al., 2016). An additional important feature of our results is the near absence of sedimentary FeOx at all sites across Wijdefjorden during the early and middle Holocene (Fig. 5), possibly resulting from very limited glacial activity during that period in agreement with significantly reduced sediment accumulation rates at that time (Fig. 2) (Allaart et al., 2020; Farnsworth et al., 2020; Jang et al., 2021). Later, the re-appearance of FeOx at the southernmost sites 1100 and 1106 reflects the regional increase in glacial activity from approximately 4 kyr BP (Farnsworth et al., 2020; Jang et al., 2020), culminating in maximum glacier extents during the last two millennia in many places on Svalbard (Jang et al., 2020, 2021).

Importantly, the time-transgressive disappearance of FeOx sedimentary layers across Wijdefjorden can be used to calculate the retreat rate of the SBIS on northern Svalbard during the last deglaciation using the following equation:

$$\text{Glacier retreat rate (m/yr)} = \frac{d_{\text{eff}} - (d_{\text{eff}} - d_{B-A})}{T_B - T_A}$$

where d_{eff} is the effective distance for iron delivery and d_{B-A} is the distance between sites B and A. T_A and T_B correspond to the timing of the disappearance of FeOx layers at sites A and B, respectively. In the case that only a single sediment core is available (such as 1085), the equation can be modified as follows:

$$\text{Glacier retreat rate (m/yr)} \leq \frac{d_{\text{eff}}}{T_f - T_i}$$

where T_f and T_i correspond to the timing of the disappearance and appearance of FeOx layers in a single sediment core. When T_i is consistent with the bottom age of the sediment core, the calculated retreat rate could be the maximum estimation. Nevertheless, the bottom age of 1085 (16.3 kyr BP) corresponds to the timing of the beginning of the SBIS retreat from the site (Hughes et al., 2016), and thus, the uncertainty for the retreat rate between 16.3 and 12.3 kyr BP based on the abundance of FeOx exclusively in core 1085 primarily relies on the assumed d_{eff} . In general, the effective distance for iron delivery, d_{eff} , is inevitably variable on the order of 10–100 km along the advective pathway (Hopwood et al., 2018). Here, we tentatively assumed d_{eff} to be 70 km during the last deglaciation based on a previous reconstruction of the SBIS extent (Farnsworth et al., 2020; Hughes et al., 2016). The assumed d_{eff} allows us to roughly estimate the SBIS extent during that time, which is generally consistent with previous reconstructions from both the DATED-1 (Hughes et al., 2016) and SVALHOLA (Farnsworth et al., 2020) (Fig. 7). On the other hand, d_{eff} during post-glacial times could have been smaller than before due to relatively reduced meltwater inputs during the late Holocene (Dowdeswell et al., 2015), as inferred from the low sediment accumulation rate (Fig. 2). For this reason, our calculation for the glacier advance rate during the late Holocene represents a maximum estimate.

The general uncertainty in calculated glacier retreat rates depends on the uncertainty in the timing of FeOx disappearance between each studied site (i.e., $T_B - T_A$; hereafter referred to as ΔT). To estimate the uncertainty in ΔT , we first collected all iterative Markov chain Monte Carlo-derived ages for a given depth during BACON simulations ($n = 6587, 7969$ and 6484 for cores 1085, 1094 and 1100, respectively). We randomly resampled age data from these databases by applying a bootstrap method (Efron and Tibshirani, 1985). The resampled ages were used for the Monte-Carlo calculation of ΔT ($n = 100,000$), and 2-sigma variability was reported for the uncertainty of ΔT in the 95% confidence interval

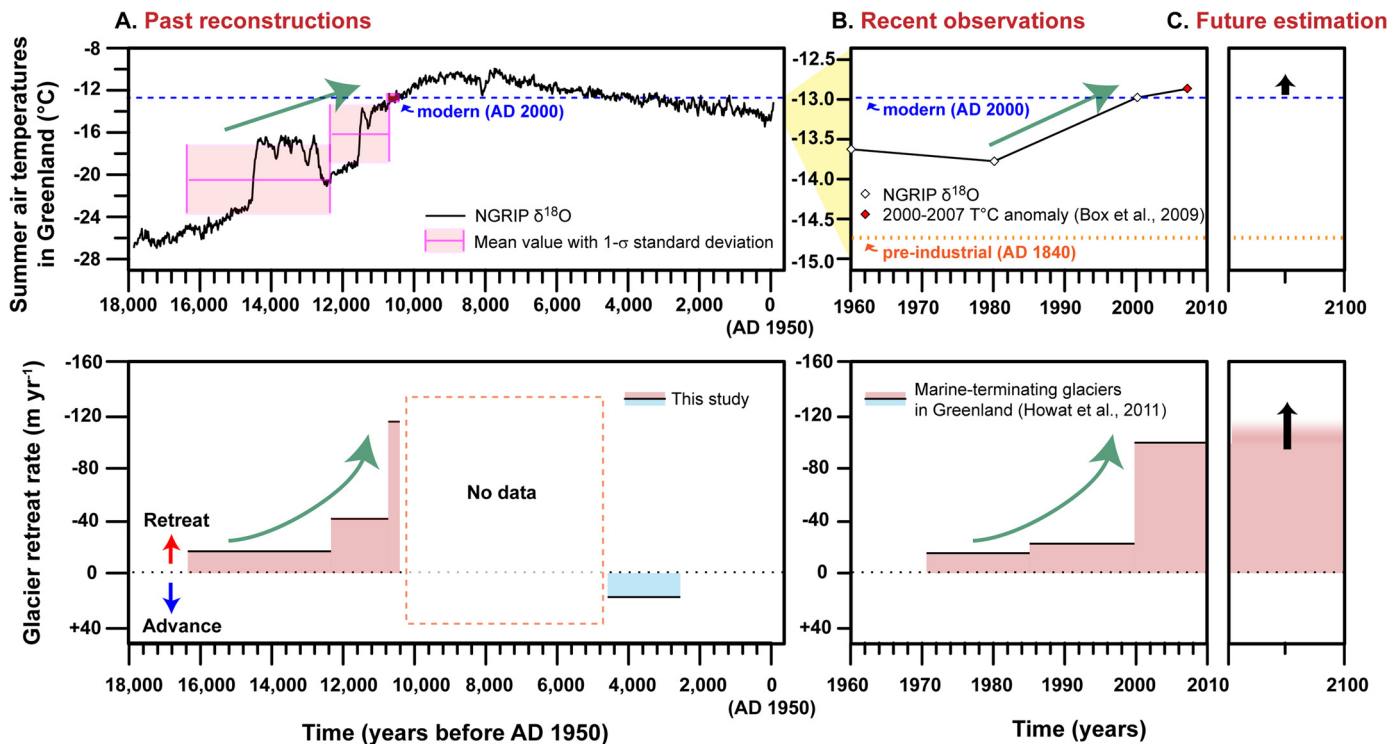


Fig. 8. Comparison of the Arctic glacier advance/retreat rates with the evolution of Greenland summer air temperatures. The overall increasing trend of the glacier retreat rate generally mimics the summer air temperature (Box et al., 2009; Buizert et al., 2018). Both past reconstructions (A) and recent observations (B) show that glacier melting rapidly increases beyond a threshold summer temperature value of approximately $+1.8^{\circ}\text{C}$ above pre-industrial value, suggesting accelerated glacier retreat in the future (C) (Pattyn et al., 2018).

(Supplementary Table S10). Because of the limited age difference between the last occurrence of FeOx at Sites 1094 and 1100 (426 yr), the relative uncertainty in ΔT is significantly higher (24~825 yr). This larger uncertainty leads to high uncertainty in the calculated glacier retreat rate during the early Holocene (10.8 and 10.4 kyr BP), ranging from -60 to -2060 m/yr (Supplementary Table S10). Note, however, that this does not affect the following conclusion regarding the timing and inferred rate of glacier melting at that time.

To summarize, our results indicate that the overall deglaciation from the continental shelf to the inner fjord occurred within ~ 5900 years between 16.3 and 10.4 kyr BP, yielding an average rate of 31 m/yr (Supplementary Table S10). In detail, however, our calculations reveal that glacier retreat rates abruptly increased from 41 to 116 m/yr at about 10.8 kyr BP (Fig. 8). The episode of accelerating glacier retreat after 10.8 kyr BP could be alternatively interpreted as possibly reflecting sustained inputs of FeOx derived from a remaining glacier within the tributary fjord (i.e., Mosselbukta; Fig. 3) to core 1094, while the main glacier draining Wijdefjorden had already retreated far into the fjord before 10.8 kyr BP. However, the catchment geology of Mosselbukta is dominated by metamorphic rocks, which do not represent a primary source of FeOx as indicated by the observed spatial variability of FeOx in Svalbard surface sediments (see Fig. 3 and also section 5.1) and hence is unlikely to have significantly influenced the evolution of sedimentary FeOx at core 1094. Therefore, the calculated acceleration of glacier retreat after 10.8 kyr BP most likely resulted from climate and environmental changes.

5.5. Non-linear response of glacier melting to global warming

Accelerating glacier retreat rates in polar regions typically result from enhanced calving and sliding associated with bathymetric deepening (Briner et al., 2009), but also with warmer ambi-

ent seawater (Holland et al., 2008) and/or the rise of atmospheric temperature (Rasmussen and Thomsen, 2021). In Wijdefjorden, bathymetry is unlikely to have played a role in the acceleration of glacier retreat during the early Holocene, because site 1085 is located at relatively deep water depth (322 m; Fig. 1) and because regional sea-level further decreased in response to isostatic rebound in northern Svalbard at that time (Forman et al., 2004). Conversely, the global increase in atmospheric and sea surface temperatures from the late Pleistocene to the early Holocene played a major role in the evolution of glacier melting (Supplementary Fig. S3). The enhanced surface and basal melting caused by atmospheric and oceanic warming possibly led to break-up of the floating tongue, resulting in the rapid disintegration of glaciers (Wood et al., 2021). In Wijdefjorden, a hydroxylated isoprenoid GDGTs sea-surface temperature (SST) record indicates a warmer seawater trend toward the early Holocene with a maximum at 11.0–9.9 and 8.3–8.1 kyr BP (Allaart et al., 2020) (Supplementary Fig. S3B). A similar SST trend has also been reconstructed using the alkenone unsaturation index in Woodfjorden (Bartels et al., 2017) (Supplementary Fig. S3C). Similarly, all temperature records reconstructed from marine and lake sediments in northwestern Svalbard uniformly indicate a general warming across the transition from the late Pleistocene to the early Holocene (van der Bilt et al., 2018; Werner et al., 2016) (Supplementary Fig. S3D & S3E). Likewise, it is well documented that Arctic air temperatures, inferred from $\delta^{18}\text{O}$ investigations of Greenland ice cores, also increased steadily during the last deglaciation (Buizert et al., 2018) (Supplementary Fig. S3F & S3G). Therefore, the rise in regional seawater and atmospheric temperatures during the last deglaciation most likely represents the main cause of the overall increase in the glacier melting rate on northern Svalbard.

The inferred temperature dependency of glacier retreat rates throughout the last deglaciation may suggest that the abrupt acceleration of glacier retreat after 10.8 kyr BP was related to an abrupt

shift towards increasing oceanic and atmospheric temperatures. However, all reconstructed temperature proxy records indicate instead a gradual deglacial warming (Supplementary Fig. S3), hence ruling out a linear response of glacier melting to increasing temperatures. A similar case comes from modern Greenland, where the retreat of hundreds of marine-terminating glaciers markedly accelerated from mean rates of 22 m/yr between 1985 and 2000 to 103 m/yr for the 2000–2010 period (Howat and Eddy, 2011), with no evidence for any dramatic temperature increase (Fig. 8). Collectively, our FeOx proxy record for early Holocene glacier retreat in Svalbard and recent decadal observations imply a non-linear relationship between glacier melting and temperature increases (Trusel et al., 2018).

5.6. Accelerated glacier melting beyond a temperature tipping point?

A striking feature of our results is that the early Holocene event of rapid deglaciation at 10.8 kyr BP occurred when summer air temperatures at the location of the North Greenland Ice Core Project (NGRIP) were comparable to AD 2000 ($\sim 1.8^\circ\text{C}$ above pre-industrial values; Buizert et al., 2018) (Fig. 8). Since the melting of the Greenland ice sheet largely occurs during the summer season (Van den Broeke et al., 2009), summer air temperature records in polar regions, rather than global temperature records such as the global mean surface temperature (e.g., Osman et al., 2021), appear to be best suited for evaluating the impact of global warming on Arctic glacier melting. One could possibly argue that the summer air temperature record from central Greenland (i.e., NGRIP; Supplementary Fig. S3F) cannot be representative of the evolution of atmospheric temperature in the maritime environment of Svalbard. Given the absence of any air temperature record for Svalbard over the last 16 kyr, other records from coastal Eastern Greenland (e.g., Zachariae Isstrom; Supplementary Fig. S3G) could be more appropriate for comparison with our proxy records. However, the hydrological setting along Eastern Greenland is strongly affected by the cold southward-flowing East Greenland Current (Fig. 1A), which results in a spatial SST distribution pattern that is decoupled from that of the West Spitsbergen Current-dominated region around Svalbard (Romanovsky et al., 2010) (Fig. 1A). Because the temperature records inferred from Eastern Greenland ice cores are likely to have been influenced by variations in the relative strength of the East Greenland Current over time (Bonnet et al., 2010), these records are probably less appropriate than the NGRIP record for comparison with Svalbard.

Based on the above, our results provide direct support that Arctic glacier melting increased markedly during the early Holocene, when summer temperatures in central Greenland reached the AD 2000 value, i.e., approximately $+1.8^\circ\text{C}$ above pre-industrial values. This particular atmospheric temperature coincides with the threshold value over which irreversible mass loss of the Greenland ice sheet has been suggested to occur at present (Pattyn et al., 2018). Such a non-linear response of glacier melting beyond a specific temperature tipping point could potentially relate to the larger exposure of ice-sheet surfaces as a result of reduced ice-sheet height led by warmer temperatures, i.e., the so-called positive melt-elevation feedback (Boers and Rypdal, 2021; Pattyn et al., 2018). Since regional summer temperatures in Greenland have already crossed that postulated tipping point and are projected to rise in the near future (Rantanen et al., 2022), our findings hence re-emphasize the prediction that global warming could cause a massive loss of glaciers and other ice masses in the Northern Hemisphere during the coming decades or centuries (Pattyn et al., 2018).

6. Conclusion

In this study, we showed that sedimentary iron (oxyhydr)oxide layers (FeOx) preserved in coastal glacial marine sediments can serve as diagnostic features of past glacial melting events. When glacial meltwater discharges into seawater, the export of glacially-derived iron fed by subglacial weathering appears to result in massive FeOx deposition in ice-proximal marine environments. The application of this new proxy to four sediment cores recovered along an ~ 150 km long transect in the longest fjords system on northern Svalbard enabled us to reconstruct the evolution of glaciers during the past 16 kyr. Our results indicate an overall increase in glacier melting rates from 18 to 41 m/yr between 16.3 and 10.8 kyr BP, attributed to the gradual rise of temperature recorded in marine sediments and ice cores. A pronounced acceleration of glacier melting rate (up to 116 m/yr) occurred in northern Svalbard after 10.8 kyr BP, which did not coincide with any change in temperature gradients. This finding implies a non-linear response of glacier melting to regional warming, which echoes what has been recently observed in Greenland, when the average retreat rates of marine-terminating glaciers abruptly increased after AD 2000. Given that both past and recent cases of accelerated glacier melting in both Svalbard and Greenland occurred when the summer air temperature in central Greenland reached $+1.8^\circ\text{C}$ above pre-industrial values, this value could represent a temperature tipping point above which glacier melting accelerates. Considering that the Arctic near-surface air temperatures currently stand at $\sim 3^\circ\text{C}$ above pre-industrial values (Rantanen et al., 2022), the future projections for massive loss of Arctic ice masses would be re-emphasized.

CRediT authorship contribution statement

Kwangchul Jang: Conceptualization, Funding acquisition, Investigation, Methodology, Visualization, Writing – original draft, Writing – review & editing. **Germain Bayon:** Conceptualization, Supervision, Writing – review & editing. **Christoph Vogt:** Investigation, Methodology, Writing – review & editing. **Matthias Forwick:** Project administration, Resources, Writing – review & editing. **Youngkyu Ahn:** Investigation, Writing – review & editing. **Jung-Hyun Kim:** Visualization, Writing – review & editing. **Seung-II Nam:** Funding acquisition, Project administration, Resources, Supervision, Writing – review & editing.

Declaration of competing interest

The authors declare that they have no known competing financial interests or personal relationships that could have appeared to influence the work reported in this paper.

Data availability

The data that support the findings of this study are available in Supplementary Information.

Acknowledgements

This study was supported mainly by the Basic Core Technology Development Program for the Oceans and the Polar Regions (NRF-2021M1A5A1075512) (KOPRI-PN23013) and the Basic Science Research Program (2017R1A6A3A01076729) from a National Research Foundation of Korea Grant from the Korean Government (MSIT; the Ministry of Science and ICT). We would like to thank all the participants of the cruises on RV *Helmer Hanssen* for their support of the core sampling, as well as D. Kim, K. Park, Y. Joe, Y. J. Joo, and Y. Son for laboratory assistance. We also thank the XRD lab crew of the Crystallography & Geomaterials group at Geosciences

Bremen for keeping the machines always online, in particular J. Birkenstock, Th. Messner, R.X. Fischer and E.M. Schmidt, and appreciate L. Allaart (GEUS in Aarhus) kindly providing bathymetric dataset in Wijdefjorden.

Appendix A. Supplementary material

Supplementary material related to this article can be found online at <https://doi.org/10.1016/j.epsl.2023.118054>.

References

- Allaart, L., Müller, J., Schomacker, A., Rydningen, T.A., Håkansson, L., Kjellman, S.E., Mollenhauer, G., Forwick, M., 2020. Late Quaternary glacier and sea-ice history of northern Wijdefjorden, Svalbard. *Boreas*.
- Bartels, M., Titschack, J., Fahl, K., Stein, R., Seidenkrantz, M.-S., Hillaire-Marcel, C., Hebbeln, D., 2017. Atlantic Water advection vs. glacier dynamics in northern Spitsbergen since early deglaciation. *Clim. Past* 13, 1717–1749.
- Blaauw, M., Christen, J.A., 2011. Flexible paleoclimate age-depth models using an autoregressive gamma process. *Bayesian Anal.* 6, 457–474.
- Boers, N., Rypdal, M., 2021. Critical slowing down suggests that the western Greenland Ice Sheet is close to a tipping point. *Proc. Natl. Acad. Sci.* 118, e2024192118.
- Bonnet, S., de Vernal, A., Hillaire-Marcel, C., Radi, T., Husum, K., 2010. Variability of sea-surface temperature and sea-ice cover in the Fram Strait over the last two millennia. *Mar. Micropaleontol.* 74, 59–74.
- Box, J.E., Yang, L., Bromwich, D.H., Bai, L.-S., 2009. Greenland ice sheet surface air temperature variability: 1840–2007. *J. Climate* 22, 4029–4049.
- Boyle, E., Edmond, J., Sholkovitz, E., 1977. The mechanism of iron removal in estuaries. *Geochim. Cosmochim. Acta* 41, 1313–1324.
- Braun, C., 2019. Late Weichselian and Holocene Glacier Dynamics and Sedimentary Processes in and North of the Wijdefjorden-Austfjorden Fjord System, North Spitsbergen. The Arctic University of Norway.
- Briner, J.P., Bini, A.C., Anderson, R.S., 2009. Rapid early Holocene retreat of a Laurentide outlet glacier through an Arctic fjord. *Nat. Geosci.* 2, 496–499.
- Buizert, C., Keisling, B., Box, J., He, F., Carlson, A., Sinclair, G., DeConto, R., 2018. Greenland-wide seasonal temperatures during the last deglaciation. *Geophys. Res. Lett.* 45, 1905–1914.
- Church, J.A., Clark, P.U., Cazenave, A., Gregory, J.M., Jevrejeva, S., Levermann, A., Merrifield, M.A., Milne, G.A., Nerem, R.S., Nunn, P.D., Payne, A.J., Pfeffer, W.T., Stammer, D., Unnikrishnan, A.S., 2013. Sea level change. In: Stocker, T.F., Qin, D., Plattner, G.-K., Tignor, M., Allen, S.K., Boschung, J., Nauels, A., Xia, Y., Bex, V., Midgley, P.M. (Eds.), *Climate Change 2013: The Physical Science Basis. Contribution of Working Group I to the Fifth Assessment Report of the Intergovernmental Panel on Climate Change*. Cambridge University Press, Cambridge, United Kingdom and New York, NY, USA, pp. 1137–1216.
- Cottier, F., Nilsen, F., Skogseth, R., Tverberg, V., Skarðhamar, J., Svendsen, H., 2010. Arctic fjords: a review of the oceanographic environment and dominant physical processes. *Geol. Soc. (Lond.) Spec. Publ.* 344, 35–50.
- Cowan, E.A., Powell, R.D., 1990. Suspended sediment transport and deposition of cyclically interlaminated sediment in a temperate glacial fjord, Alaska, USA. *Geol. Soc. (Lond.) Spec. Publ.* 53, 75–89.
- Dallmann, W., Elvevold, S., 2015. Bedrock geology. In: *Geoscience Atlas of Svalbard*, vol. 148. Norsk Polarinstitutt, Tromsø, pp. 133–173.
- Dowdeswell, J.A., Hogan, K.A., Arnold, N.S., Mugford, R.I., Wells, M., Hirst, J.P.P., Decalf, C., 2015. Glacial-rich meltwater plumes and ice-proximal fans at the margins of modern and ancient tidewater glaciers: observations and modelling. *Sedimentology* 62, 1665–1692.
- Efron, B., Tibshirani, R., 1985. The bootstrap method for assessing statistical accuracy. *Behaviormetrika* 12, 1–35.
- Farnsworth, W.R., Allaart, L., Ingólfsson, Ó., Alexanderson, H., Forwick, M., Noormets, R., Retelle, M., Schomacker, A., 2020. Holocene glacial history of Svalbard: status, perspectives and challenges. *Earth-Sci. Rev.* 208, 103249.
- Flanner, M.G., Shell, K.M., Barlage, M., Perovich, D.K., Tschudi, M., 2011. Radiative forcing and albedo feedback from the Northern Hemisphere cryosphere between 1979 and 2008. *Nat. Geosci.* 4, 151–155.
- Forman, S., Lubinski, D., Ingólfsson, Ó., Zeeberg, J., Snyder, J., Siegert, M., Matishov, G., 2004. A review of postglacial emergence on Svalbard, Franz Josef Land and Novaya Zemlya, northern Eurasia. *Quat. Sci. Rev.* 23, 1391–1434.
- Fuentes, V., Alurralde, G., Meyer, B., Aguirre, G.E., Canepa, A., Wöfl, A.-C., Hass, H.C., Williams, G.N., Schloss, I.R., 2016. Glacial melting: an overlooked threat to Antarctic krill. *Sci. Rep.* 6, 27234.
- Hawkins, J.R., Wadham, J.L., Tranter, M., Raiswell, R., Benning, L.G., Statham, P.J., Tedstone, A., Nienow, P., Lee, K., Telling, J., 2014. Ice sheets as a significant source of highly reactive nanoparticulate iron to the oceans. *Nat. Commun.* 5, 1–8.
- Hawkins, J.R., Skidmore, M.L., Wadham, J.L., Prisco, J.C., Morton, P.L., Hatton, J.E., Gardner, C.B., Kohler, T.J., Stibal, M., Bagshaw, E.A., 2020. Enhanced trace element mobilization by Earth's ice sheets. *Proc. Natl. Acad. Sci.* 117, 31648–31659.
- Holland, D.M., Thomas, R.H., de Young, B., Ribergaard, M.H., Lyberth, B., 2008. Acceleration of Jakobshavn Isbræ triggered by warm subsurface ocean waters. *Nat. Geosci.* 1, 659–664.
- Hopwood, M.J., Carroll, D., Browning, T., Meire, L., Mortensen, J., Krisch, S., Achterberg, E.P., 2018. Non-linear response of summertime marine productivity to increased meltwater discharge around Greenland. *Nat. Commun.* 9, 1–9.
- Horton, B.P., Khan, N.S., Cahill, N., Lee, J.S., Shaw, T.A., Garner, A.J., Kemp, A.C., Engelhart, S.E., Rahmstorf, S., 2020. Estimating global mean sea-level rise and its uncertainties by 2100 and 2300 from an expert survey. *npj Clim. Atmos. Sci.* 3, 1–8.
- Howat, I.M., Eddy, A., 2011. Multi-decadal retreat of Greenland's marine-terminating glaciers. *J. Glaciol.* 57, 389–396.
- Hughes, A.L., Gyllencreutz, R., Lohne, ØS., Mangerud, J., Svendsen, J.I., 2016. The last Eurasian ice sheets—a chronological database and time-slice reconstruction, DATED-1. *Boreas* 45, 1–45.
- Isaksen, K., Benestad, R., Harris, C., Solli, J., 2007. Recent extreme near-surface permafrost temperatures on Svalbard in relation to future climate scenarios. *Geophys. Res. Lett.* 34, L17502.
- Jakobsson, M., Mayer, L.A., Bringenspar, C., Castro, C.F., Mohammad, R., Johnson, P., Ketter, T., Accettella, D., Amblas, D., An, L., Arndt, J.E., Canals, M., Casamor, J.L., Chauché, N., Coakley, B., Danielson, S., Demarte, M., Dickson, M.-L., Dorschel, B., Dowdeswell, J.A., Dreutter, S., Fremand, A.C., Gallant, D., Hall, J.K., Hehemann, L., Hodnesdal, H., Hong, J., Ivaldi, R., Kane, E., Klauke, I., Krawczyk, D.W., Kristoffersen, Y., Kuipers, B.R., Millan, R., Masetti, G., Morlighem, M., Noormets, R., Prescott, M.M., Rebesco, M., Rignot, E., Semiletov, I., Tate, A.J., Travaglini, P., Velicogna, I., Weatherall, P., Weinreb, W., Willis, J.K., Wood, M., Zarayskaya, Y., Zhang, T., Zimmermann, M., Zinglersen, K.B., 2020. The international bathymetric chart of the Arctic Ocean version 4.0. *Sci. Data* 7, 176.
- Jang, K., Bayon, G., Han, Y., Joo, Y.J., Kim, J.-H., Ryu, J.-S., Woo, J., Forwick, M., Szczuciński, W., Kim, J.-H., Nam, S.-I., 2020. Neodymium isotope constraints on chemical weathering and past glacial activity in Svalbard. *Earth Planet. Sci. Lett.* 542, 116319.
- Jang, K., Ahn, Y., Joe, Y.J., Braun, C.A., Joo, Y.J., Kim, J.-H., Bayon, G., Forwick, M., Vogt, C., Nam, S.-I., 2021. Glacial and environmental changes in northern Svalbard over the last 16.3 ka inferred from neodymium isotopes. *Glob. Planet. Change* 201, 103483.
- Kanna, N., Sugiyama, S., Fukamachi, Y., Nomura, D., Nishioka, J., 2020. Iron supply by subglacial discharge into a fjord near the front of a marine-terminating glacier in Northwestern Greenland. *Glob. Biogeochem. Cycles* 34, e2020GB006567.
- Knies, J., Martinez, P., 2009. Organic matter sedimentation in the western Barents Sea region: terrestrial and marine contribution based on isotopic composition and organic nitrogen content. *Norwegian J. Geol.* 89, 79–89.
- Kochitzky, W., Copland, L., Van Wychen, W., Hugonnet, R., Hock, R., Dowdeswell, J.A., Benham, T., Strozzi, T., Glazovsky, A., Lavrentiev, I., Rounce, D.R., Millan, R., Cook, A., Dalton, A., Jiskoot, H., Cooley, J., Jania, J., Navarro, F., 2022. The unquantified mass loss of Northern Hemisphere marine-terminating glaciers from 2000–2020. *Nat. Commun.* 13, 5835.
- Laufer-Meiser, K., Michaud, A.B., Maisch, M., Byrne, J.M., Kappler, A., Patterson, M.O., Røy, H., Jørgensen, B.B., 2021. Potentially bioavailable iron produced through benthic cycling in glaciated Arctic fjords of Svalbard. *Nat. Commun.* 12, 1–13.
- Lindsay, R., Schweiger, A., 2015. Arctic sea ice thickness loss determined using sub-surface, aircraft, and satellite observations. *Cryosphere* 9, 269–283.
- Mangerud, J., Bondevik, S., Gulliksen, S., Karin Hufthammer, A., Høisæter, T., 2006. Marine ¹⁴C reservoir ages for 19th century whales and molluscs from the North Atlantic. *Quat. Sci. Rev.* 25, 3228–3245.
- Meslard, F., Bourrin, F., Many, G., Kerhervé, P., 2018. Suspended particle dynamics and fluxes in an Arctic fjord (Kongsfjorden, Svalbard). *Estuar. Coast. Shelf Sci.* 204, 212–224.
- Ó Cofaigh, C., Dowdeswell, J.A., 2001. Laminated sediments in glacial marine environments: diagnostic criteria for their interpretation. *Quat. Sci. Rev.* 20, 1411–1436.
- Oppenheimer, M., Glavovic, B., Hinkel, J., van de Wal, R., Magnan, A.K., Abd-Elgawad, A., Cai, R., Cifuentes-Jara, M., Deconto, R.M., Ghosh, T., 2019. Sea level rise and implications for low lying islands, coasts and communities. In: Pörtner, H.-O., et al. (Eds.), *IPCC Special Report on the Ocean and Cryosphere in a Changing Climate*.
- Osman, M.B., Tierney, J.E., Zhu, J., Tardif, R., Hakim, G.J., King, J., Poulsen, C.J., 2021. Globally resolved surface temperatures since the Last Glacial Maximum. *Nature* 599, 239–244.
- Pattyn, F., Ritz, C., Hanna, E., Asay-Davis, X., DeConto, R., Durand, G., Favier, L., Fettweis, X., Goelzer, H., Gollledge, N.R., 2018. The Greenland and Antarctic ice sheets under 1.5°C global warming. *Nat. Clim. Change* 8, 1053–1061.
- Petschick, R., Kuhn, G., Ginge, F., 1996. Clay mineral distribution in surface sediments of the South Atlantic: sources, transport, and relation to oceanography. *Mar. Geol.* 130, 203–229.
- Raiswell, R., Hawkins, J., Elsenousy, A., Death, R., Tranter, M., Wadham, J., 2018. Iron in glacial systems: speciation, reactivity, freezing behavior, and alteration during transport. *Front. Earth Sci.* 6.
- Rantanen, M., Karpechko, A.Y., Lipponen, A., Nordling, K., Hyvärinen, O., Ruosteenoja, K., Vihma, T., Laaksonen, A., 2022. The Arctic has warmed nearly four times faster than the globe since 1979. *Commun. Earth Environ.* 3, 168.

- Rasmussen, T.L., Thomsen, E., 2021. Climate and ocean forcing of ice-sheet dynamics along the Svalbard-Barents Sea ice sheet during the deglaciation ~20, 000–10, 000 years BP. *Quat. Sci. Adv.* 3, 100019.
- Raven, M.D., Self, P.G., 2017. Outcomes of 12 years of the Reynolds Cup quantitative mineral analysis round robin. *Clays Clay Miner.* 65, 122–134.
- Romanovsky, V.E., Smith, S.L., Christiansen, H.H., 2010. Permafrost thermal state in the polar Northern Hemisphere during the international polar year 2007–2009: a synthesis. *Permafrost. Periglac.* 21, 106–116.
- Rye, C.D., Naveira Garabato, A.C., Holland, P.R., Meredith, M.P., George Nurser, A.J., Hughes, C.W., Coward, A.C., Webb, D.J., 2014. Rapid sea-level rise along the Antarctic margins in response to increased glacial discharge. *Nat. Geosci.* 7, 732–735.
- Schroth, A.W., Crusius, J., Hoyer, I., Campbell, R., 2014. Estuarine removal of glacial iron and implications for iron fluxes to the ocean. *Geophys. Res. Lett.* 41, 3951–3958.
- Shepherd, A., Ivins, E., Rignot, E., Smith, B., van den Broeke, M., Velicogna, I., Whitehouse, P., Briggs, K., Joughin, I., Krinner, G., Nowicki, S., Payne, T., Scambos, T., Schlegel, N., Geruo, A., Agosta, C., Ahlström, A., Babonis, G., Barletta, V., Blazquez, A., Bonin, J., Csatho, B., Cullather, R., Felikson, D., Fettweis, X., Forsberg, R., Gallee, H., Gardner, A., Gilbert, L., Groh, A., Gunter, B., Hanna, E., Harig, C., Helm, V., Horvath, A., Horwath, M., Khan, S., Kjeldsen, K.K., Konrad, H., Langen, P., Lecavalier, B., Loomis, B., Luthcke, S., McMillan, M., Melini, D., Mernild, S., Mohajerani, Y., Moore, P., Mouginot, J., Moyano, G., Muir, A., Nagler, T., Nield, G., Nilsson, J., Noel, B., Otsuka, I., Pattle, M.E., Peltier, W.R., Pie, N., Rietbroek, R., Rott, H., Sandberg-Sørensen, L., Sasgen, I., Save, H., Scheuchl, B., Schrama, E., Schröder, L., Seo, K.-W., Simonsen, S., Slater, T., Spada, G., Sutterley, T., Talpe, M., Tarasov, L., van de Berg, W.J., van der Wal, W., van Wessem, M., Vishwakarma, B.D., Wiese, D., Wouters, B., The, I.T., 2018. Mass balance of the Antarctic Ice Sheet from 1992 to 2017. *Nature* 558, 219–222.
- Stuiver, M., Reimer, P.J., 1993. Extended ^{14}C data base and revised CALIB 3.0 ^{14}C age calibration program. *Radiocarbon* 35, 215–230.
- Svendsen, J.I., Mangerud, J., 1997. Holocene glacial and climatic variations on Spitsbergen, Svalbard. *Holocene* 7, 45–57.
- Tessin, A., März, C., Blais, M.-A., Brumsack, H.-J., Matthiessen, J., O'Regan, M., Schnetger, B., 2020. Arctic continental margin sediments as possible Fe and Mn sources to seawater as sea ice retreats: insights from the Eurasian margin. *Glob. Biogeochem. Cycles* 34, e2020GB006581.
- Trusel, L.D., Das, S.B., Osman, M.B., Evans, M.J., Smith, B.E., Fettweis, X., McConnell, J.R., Noël, B.P., van den Broeke, M.R., 2018. Nonlinear rise in Greenland runoff in response to post-industrial Arctic warming. *Nature* 564, 104–108.
- Van den Broeke, M., Bamber, J., Ettema, J., Rignot, E., Schrama, E., van de Berg, W.J., van Meijgaard, E., Velicogna, I., Wouters, B., 2009. Partitioning recent Greenland mass loss. *Science* 326, 984–986.
- van der Bilt, W.G.M., D'Andrea, W.J., Bakke, J., Balascio, N.L., Werner, J.P., Gjerde, M., Bradley, R.S., 2018. Alkenone-based reconstructions reveal four-phase Holocene temperature evolution for High Arctic Svalbard. *Quat. Sci. Rev.* 183, 204–213.
- Vogt, C., Lauterjung, J., Fischer, R.X., 2002. Investigation of the clay fraction ($< 2 \mu\text{m}$) of the clay minerals society reference clays. *Clays Clay Miner.* 50, 388–400.
- Wadham, J.L., Hawkings, J.R., Tarasov, L., Gregoire, L.J., Spencer, R.G.M., Gutjahr, M., Ridgwell, A., Kohfeld, K.E., 2019. Ice sheets matter for the global carbon cycle. *Nat. Commun.* 10, 3567.
- Wehrmann, L.M., Formolo, M.J., Owens, J.D., Raiswell, R., Ferdelman, T.G., Riedinger, N., Lyons, T.W., 2014. Iron and manganese speciation and cycling in glacially influenced high-latitude fjord sediments (West Spitsbergen, Svalbard): evidence for a benthic recycling-transport mechanism. *Geochim. Cosmochim. Acta* 141, 628–655.
- Werner, A., 1993. Holocene moraine chronology, Spitsbergen, Svalbard: lichenometric evidence for multiple Neoglacial advances in the Arctic. *Holocene* 3, 128–137.
- Werner, K., Müller, J., Husum, K., Spielhagen, R.F., Kandiano, E.S., Polyak, L., 2016. Holocene sea subsurface and surface water masses in the Fram Strait – comparisons of temperature and sea-ice reconstructions. *Quat. Sci. Rev.* 147, 194–209.
- Williams, G.D., Herraiz-Borreguero, L., Roquet, F., Tamura, T., Ohshima, K.I., Fukamachi, Y., Fraser, A.D., Gao, L., Chen, H., McMahon, C.R., Harcourt, R., Hindell, M., 2016. The suppression of Antarctic bottom water formation by melting ice shelves in Prydz Bay. *Nat. Commun.* 7, 12577.
- Wood, M., Rignot, E., Fenty, I., An, L., Bjørk, A., van den Broeke, M., Cai, C., Kane, E., Menemenlis, D., Millan, R., Morlighem, M., Mouginot, J., Noël, B., Scheuchl, B., Velicogna, I., Willis, J.K., Zhang, H., 2021. Ocean forcing drives glacier retreat in Greenland. *Sci. Adv.* 7, eaba7282.
- Zemp, M., Huss, M., Thibert, E., Eckert, N., McNabb, R., Huber, J., Barandun, M., Machguth, H., Nussbaumer, S.U., Gärtner-Roer, I., Thomson, L., Paul, F., Mausson, F., Kutuzov, S., Cogley, J.G., 2019. Global glacier mass changes and their contributions to sea-level rise from 1961 to 2016. *Nature* 568, 382–386.
- Zhang, R., John, S.G., Zhang, J., Ren, J., Wu, Y., Zhu, Z., Liu, S., Zhu, X., Marsay, C.M., Wenger, F., 2015. Transport and reaction of iron and iron stable isotopes in glacial meltwaters on Svalbard near Kongsfjorden: from rivers to estuary to ocean. *Earth Planet. Sci. Lett.* 424, 201–211.